

Non-Hermitian Hamiltonian Approach for Two-Dimensional Spectroscopy

Hao-Yue Zhang,^{†,‡} Bin-Yao Huang,^{†,‡,¶} Jing-Yi-Ran Jin,^{†,‡} Yi-Xuan Yao,^{†,‡} and
Qing Ai^{*,†,‡}

[†]*School of Physics and Astronomy, Applied Optics Beijing Area Major Laboratory, Beijing
Normal University, Beijing 100875, China*

[‡]*Key Laboratory of Multiscale Spin Physics, Ministry of Education, Beijing Normal
University, Beijing, China*

[¶]*School of Science, Chongqing University of Posts and Telecommunications, Chongqing
400065, China*

E-mail: aiqing@bnu.edu.cn

Abstract

Two-dimensional spectroscopy (2DS) offers significant advantages in terms of high temporal and frequency resolutions and signal-to-noise ratio. Until now, the response-function (RF) formalism has been the prevalent theoretical description. In this study, we compare the non-Hermitian Hamiltonian (NHH) method with the RF formalism in a three-level system with a constant control field. We obtain the signals from both approaches and compare their population dynamics and 2DS. We propose the quasi-Green function for the NHH method, which allows all possible Liouville paths to be inferred. Although the NHH method overestimates relaxations, it also provides a more comprehensive description. Our results demonstrate that the NHH method is more suitable than the RF formalism for investigating the systems that are either dissipative or complex via the 2DS.

Introduction

Two-dimensional spectroscopy (2DS) is a technique that applies sequential pulses to materials or biological systems and receives output signals rich in structural and dynamic information.¹⁻⁴ This technique is implemented with a wide range of pulse wavelengths, from UV to microwave, providing temporal resolutions ranging from milliseconds to attoseconds.⁵⁻⁹ It is widely employed in physical chemistry, condensed-matter physics, and biophysics for exploring phenomena such as energy transfer,¹⁰⁻¹³ molecular vibrations,^{14,15} electronic transitions and relaxation,¹⁶⁻¹⁸ and chemical reactions,^{19,20} as well as structures like proteins.^{21,22} The means to implement 2DS experimentally are diverse.²³⁻²⁸ The common principle involves the application of pulse sequences with different time intervals to samples, in which the pulses are well separated. The emitted polarization signals are projected onto two independent frequency axes, creating a map known as 2DS.

On the other hand, the most widely-used method for the theoretical description of the 2DS is the response-function (RF) formalism.²⁹⁻³¹ This approach employs the response functions, each corresponding to a Liouville path, to describe the polarization. The signals are viewed as the responses to the perturbations induced by the three applied pulses. However, it may overlook some Liouville paths if the system setup is complex. For example, an additional field is applied to induce transitions in the system. It may become exhausting to draw all the possible paths, although most of them do not contribute significantly. On the other hand, the non-Hermitian Hamiltonian (NHH) method, which is widely-used in investigating PT symmetry,³²⁻³⁴ photosynthetic light harvesting,³⁵⁻³⁷ chemical reaction and avian compass,³⁸⁻⁴⁰ and negative refraction in Möbius molecules,⁴¹ may overcome these disadvantages. By omitting the quantum-jump terms, it obtains a reliable solution to the quantum master equation and thus achieves a balance between computational difficulty and comprehensive description.⁴² Nevertheless, working with non-Hermitian operators still requires careful consideration in interpreting the physical processes underlying the results.

In this article, we compare the NHH method and the RF formalism in a three-level sys-

tem with a constantly-applied control field. Although Lemmer et al. first applied the NHH method to 2DS,⁴² they did not focus on the approach itself but rather on its application to study ion Coulomb crystals. In contrast, our work concentrates on the similarities and differences between these two methods in calculating 2DS. We validate their consistency by comparing the 2DS when they follow identical Liouville paths. We discuss their respective advantages and disadvantages, as well as their scopes of application. Particularly, we propose the quasi-Green function for interpreting the 2DS by the NHH method, which significantly simplifies the analytical challenges. Overall, we believe that the NHH method provides a reliable description for 2DS, particularly in complex systems, and can overcome the limitations of the RF formalism in these scenarios.

We first illustrate the RF formalism and the NHH method, in which the quasi-Green function is proposed as a counterpart to the Green function in the RF formalism. We then present their double-sided Feynman diagrams and the analytical expressions of the rephasing (RP) signal. We further provide a comparison of the Green and quasi-Green functions, the population dynamics, the conservation of the population and the 2DS by the two approaches, focusing mainly on their differences in coherent and incoherent behavior. The advantages and disadvantages, as well as the difference and consistency of the two methods are discussed. Finally, we summarize our results and offer a perspective on the application of the NHH method.

Theoretical approaches

Response Function Formalism

We consider a three-level system including a ground state $|b\rangle$, an excited state $|e\rangle$, and a metastable state $|c\rangle$, as shown in Fig. 1(a). The control field with Rabi frequency Ω_c is constantly applied to the system. When a probe field is introduced, the electromagnetically-induced transparency (EIT) effect is formed to suppress the dissipation due to quantum

interference.⁴³ For 2DS, three incident pulses of the probe field induce the $|b\rangle \leftrightarrow |e\rangle$ transition with Rabi frequency Ω_p , and the signals to be measured are emitted from the system in a specific direction, as shown in Fig. 1(b). Between the energy levels b and e , there exist bidirectional relaxations with a downhill rate Γ_1 and an uphill rate Γ_2 . Basically, the Hamiltonian of the system without probe and control fields is

$$H_0 = \sum_j \omega_j |j\rangle \langle j|, \quad (1)$$

($j = b, e, c$) where we assume $\hbar = 1$ for simplicity. Therefore, the interaction Hamiltonian under the control field is written as

$$H_{\text{int}} = \Omega_c |e\rangle \langle c| + \text{h.c.} \quad (2)$$

where $\Omega_c = -\frac{1}{2}\Omega_{ec}e^{-i\nu_c t}$ with Ω_{ec} and ν_c being the Rabi frequency and the frequency of the control field respectively. Generally speaking, the probe pulses are strong but short enough to be considered perturbations to the system.

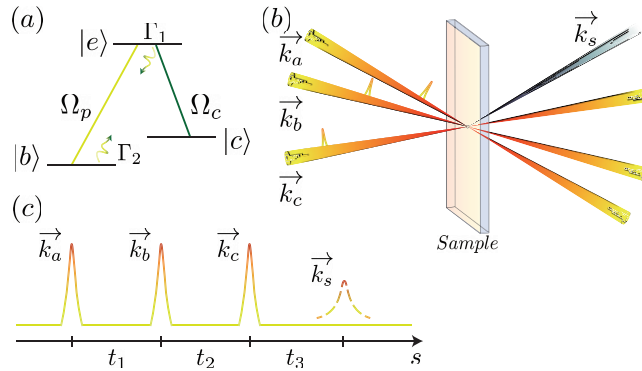


Figure 1: (a) Schematic diagram of the three-level system. The energy levels b , e and c are the ground, the excited and the metastable states, respectively. The probe pulses denoted as the light-green line are applied to induce the $|b\rangle \leftrightarrow |e\rangle$ transition with Rabi frequency Ω_p ($p = a, b, c$), and the control field denoted as the dark-green line is resonantly coupled to the $|e\rangle \leftrightarrow |c\rangle$ transition with Rabi frequency Ω_{ec} . (b) Three probe pulses and the signal. (c) Sequence of pulses and signal, in which t_1 , t_2 and t_3 are respectively the time intervals between two adjacent pulses. The dashed line represents the emitted signal.

The 2DS are plotted using the third-order response function after double Fourier trans-

formation. This function is proportional to the intensity of third-order polarization $\langle \mu \rho^{(3)}(t) \rangle$ and is expressed as

$$S^{(3)}(t_3, t_2, t_1) = (-i)^3 \times \langle \mu(t_3 + t_2 + t_1) [\mu(t_2 + t_1), [\mu(t_1), [\mu(0), \rho(0)]]] \rangle, \quad (3)$$

where t_1 , t_2 and t_3 are the time intervals between two adjacent pulses, as shown in Fig. 1(c). $\rho(0)$ represents the initial equilibrium state under the Hamiltonian H_0 , while $\mu(s) = e^{iH_0 s} \mu e^{-iH_0 s}$ is the dipole operator in the interaction picture. By expanding the commutators, the third-order polarization is divided into eight terms with

$$\begin{aligned} R_1 &= \langle \mu(t_3 + t_2 + t_1) \mu(0) \rho(0) \mu(t_1) \mu(t_2 + t_1) \rangle, \\ R_2 &= \langle \mu(t_3 + t_2 + t_1) \mu(t_1) \rho(0) \mu(0) \mu(t_2 + t_1) \rangle, \\ R_3 &= \langle \mu(t_3 + t_2 + t_1) \mu(t_2 + t_1) \rho(0) \mu(0) \mu(t_1) \rangle, \\ R_4 &= \langle \mu(t_3 + t_2 + t_1) \mu(t_2 + t_1) \mu(t_1) \mu(0) \rho(0) \rangle. \end{aligned} \quad (4)$$

and their hermitian conjugates. The incidence of three probe pulses from different directions allows for selective observation of certain combinations of the eight terms mentioned above. For example, the RP signal is emitted in the direction $\vec{k}_s = -\vec{k}_a + \vec{k}_b + \vec{k}_c$ as

$$S_{\text{RP}}^{(3)}(\omega_3, t_2, \omega_1) \propto \text{Re} [R_2(\omega_3, t_2, \omega_1) + R_3(\omega_3, t_2, \omega_1)]. \quad (5)$$

R_n ($n = 1, 2, 3, 4$) and their hermitian conjugates, can be obtained by solving the quantum master equation. This equation describes quantum dynamics of the open system and is

written as

$$\begin{aligned}\dot{\rho} = & -i[H, \rho] - \Gamma_1 \mathfrak{L}(A_{be}) \rho - \Gamma_2 \mathfrak{L}(A_{eb}) \rho \\ & - \sum_j \gamma_j^{(0)} \mathfrak{L}(A_{jj}) \rho,\end{aligned}\quad (6)$$

where $A_{ij} = |i\rangle\langle j|$ is the quantum jump operator describing the process of jumping from $|j\rangle$ to $|i\rangle$, $\gamma_j^{(0)}$ is the pure-dephasing noise for each state, and $\mathfrak{L}(A_{ij}) \rho = \frac{1}{2} \{A_{ij}^\dagger A_{ij}, \rho\} - A_{ij} \rho A_{ij}^\dagger$ with $\{A_{ij}^\dagger A_{ij}, \rho\} = A_{ij}^\dagger A_{ij} \rho + \rho A_{ij}^\dagger A_{ij}$ being the anti-commutator. Assuming that the control field is in resonance with the $|e\rangle \leftrightarrow |c\rangle$ transition, the time evolution of the elements of the density matrix in the interaction picture are as follows

$$\begin{aligned}\dot{\rho}_{bb} &= \Gamma_1 \rho_{ee} - \Gamma_2 \rho_{bb}, \\ \dot{\rho}_{ee} &= \frac{i}{2} \Omega_{ec} (\rho_{ce} - \rho_{ec}) - \Gamma_1 \rho_{ee} + \Gamma_2 \rho_{bb}, \\ \dot{\rho}_{cc} &= -\frac{i}{2} \Omega_{ec} (\rho_{ce} - \rho_{ec}), \\ \dot{\rho}_{eb} &= \frac{i}{2} \Omega_{ec} \rho_{cb} - \gamma_{eb} \rho_{eb}, \\ \dot{\rho}_{be} &= -\frac{i}{2} \Omega_{ec} \rho_{bc} - \gamma_{eb} \rho_{be}, \\ \dot{\rho}_{ec} &= \frac{i}{2} \Omega_{ec} (\rho_{cc} - \rho_{ee}) - \gamma_{ec}^+ \rho_{ec}, \\ \dot{\rho}_{ce} &= -\frac{i}{2} \Omega_{ec} (\rho_{cc} - \rho_{ee}) - \gamma_{ec}^+ \rho_{ce}, \\ \dot{\rho}_{cb} &= \frac{i}{2} \Omega_{ec} \rho_{eb} - \gamma_{bc} \rho_{cb}, \\ \dot{\rho}_{bc} &= -\frac{i}{2} \Omega_{ec} \rho_{be} - \gamma_{bc} \rho_{bc},\end{aligned}\quad (7)$$

where the dissipation of the energy level c is neglected, and the dephasing rates read

$$\gamma_{eb} = \frac{1}{2} \left(\Gamma_1 + \Gamma_2 + \gamma_e^{(0)} + \gamma_b^{(0)} \right), \quad (8)$$

$$\gamma_{ec}^+ = \frac{1}{2} \left(\Gamma_1 + \gamma_e^{(0)} + \gamma_c^{(0)} \right), \quad (9)$$

$$\gamma_{bc} = \frac{1}{2} \left(\Gamma_2 + \gamma_b^{(0)} + \gamma_c^{(0)} \right). \quad (10)$$

Using the Green functions to further describe the time evolution of the density matrix elements, the RP signal is written in a more specific form⁴⁴

$$\begin{aligned}
S_{\text{RP}}^{(3)}(\omega_3, t_2, \omega_1) = & \tilde{\mathcal{G}}_{ebeb}(\omega_3)\mathcal{G}_{eeee}(t_2)\tilde{\mathcal{G}}_{bebe}(\omega_1) \\
& + \tilde{\mathcal{G}}_{ebeb}(\omega_3)\mathcal{G}_{bbee}(t_2)\tilde{\mathcal{G}}_{bebe}(\omega_1) \\
& + \tilde{\mathcal{G}}_{ebeb}(\omega_3)\mathcal{G}_{eebb}(t_2)\tilde{\mathcal{G}}_{bebe}(\omega_1) \\
& + \tilde{\mathcal{G}}_{ebeb}(\omega_3)\mathcal{G}_{bbbb}(t_2)\tilde{\mathcal{G}}_{bebe}(\omega_1),
\end{aligned} \tag{11}$$

where the Green function $\mathcal{G}_{ijkl}(t) = \rho_{ij}(t)$ for the initial condition $\rho_{mn}(0) = \delta_{mk}\delta_{nl}$. The double-sided Feynman diagrams for each term in Eq. (11) are shown in Fig. 2, with (a), (b), (c) and (d) corresponding to four terms in turn. The evolutions during t_2 with the initial and final states are explicitly demonstrated in the diagrams. The first and the last terms of Eq. (11) respectively correspond to R_2 and R_3 in Eq. (4). The other two terms, however, do not correspond to R_n because they are induced by the population transfer during t_2 . The evolution of the non-diagonal elements in t_1 and t_3 are described by the Green functions as

$$\begin{aligned}
\tilde{\mathcal{G}}_{bebe}(\omega_1) &= \frac{4(\omega_1 - i\gamma_{bc} - \omega_{eb})}{4(\omega_1 - i\gamma_{bc} - \omega_{eb})(\omega_1 - i\gamma_{eb} - \omega_{eb}) - \Omega_{ec}^2}, \\
\tilde{\mathcal{G}}_{ebeb}(\omega_3) &= \frac{4(\omega_3 + i\gamma_{bc} - \omega_{eb})}{4(\omega_3 + i\gamma_{bc} - \omega_{eb})(\omega_3 + i\gamma_{eb} - \omega_{eb}) - \Omega_{ec}^2},
\end{aligned} \tag{12}$$

while the evolution in t_2 is obtained by assuming two possible initial states after the first

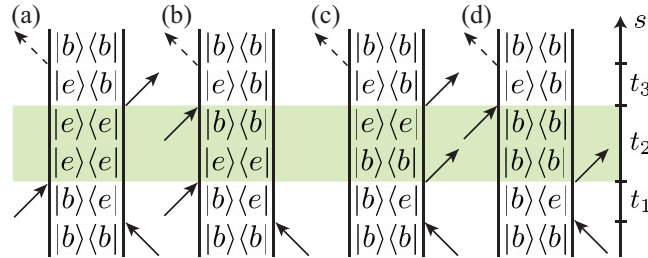


Figure 2: Feynman diagrams of the three-level system by the RF formalism. (a), (b), (c) and (d) demonstrate the four Liouville paths of the RP signal, i.e., the four terms in Eq. (11). The evolution during t_2 is highlighted.

two pulses. In the situation where the system is at $|e\rangle$ at the beginning of the population time, the Green functions for the system to remain at $|e\rangle$ or to evolve to $|b\rangle$ are respectively written as

$$\begin{aligned} \mathcal{G}_{eeee}(t_2) = & e^{-\frac{1}{2}\gamma_{ec}^+ t_2} \left[\frac{A_2 \Gamma_2 \gamma_{ec} + \Omega_{ec}^2 (\gamma_{ec} - 2\Gamma_1)}{4\tilde{\Omega}_+ A_1} \sin \tilde{\Omega}_+ t_2 \right. \\ & \left. + \frac{A_2 \Gamma_2 + \Omega_{ec}^2}{2A_1} \cos \tilde{\Omega}_+ t_2 \right] + \frac{\Gamma_2}{2(\Gamma_1 + \Gamma_2)} \\ & + \frac{\Gamma_1 (2A_1 - \Omega_{ec}^2)}{2A_1 (\Gamma_1 + \Gamma_2)} e^{-(\Gamma_1 + \Gamma_2)t_2}, \end{aligned} \quad (13)$$

$$\begin{aligned} \mathcal{G}_{bbee}(t_2) = & e^{-\frac{1}{2}\gamma_{ec}^+ t_2} \Gamma_1 \left[\frac{A_2 \gamma_{ec}^+ + 2\Omega_{ec}^2}{4\tilde{\Omega}_+ A_1} \sin \tilde{\Omega}_+ t_2 \right. \\ & \left. + \frac{A_2}{2A_1} \cos \tilde{\Omega}_+ t_2 \right] + \frac{\Gamma_1}{2(\Gamma_1 + \Gamma_2)} \\ & - \frac{\Gamma_1 (2A_1 - \Omega_{ec}^2)}{2A_1 (\Gamma_1 + \Gamma_2)} e^{-(\Gamma_1 + \Gamma_2)t_2}, \end{aligned} \quad (14)$$

where

$$A_1 = (\Gamma_1 + \Gamma_2) (\Gamma_1 + \Gamma_2 - \gamma_{ec}^+) + \Omega_{ec}^2, \quad (15)$$

$$A_2 = \Gamma_1 + \Gamma_2 - \gamma_{ec}^+, \quad (16)$$

$$\tilde{\Omega}_+ = \sqrt{\Omega_{ec}^2 - \frac{1}{4}(\gamma_{ec}^+)^2}. \quad (17)$$

Similarly, in the other situation where the system is still at $|b\rangle$ after excitation, the Green functions are written as

$$\mathcal{G}_{ecbb}(t_2) = \frac{\Gamma_2 - \Gamma_2 e^{-(\Gamma_1 + \Gamma_2)t_2}}{\Gamma_1 + \Gamma_2}, \quad (18)$$

$$\mathcal{G}_{bbbb}(t_2) = \frac{\Gamma_1 + \Gamma_2 e^{-(\Gamma_1 + \Gamma_2)t_2}}{\Gamma_1 + \Gamma_2}. \quad (19)$$

Eventually, by taking the real part of the double Fourier transformed response function, the RP signal and thus the 2DS are obtained.

non-Hermitian Hamiltonian method

We apply the NHH method to the same system in Fig. 1(a). Starting directly from the master Eq. (6), we drop the quantum-jump term and approximately obtain

$$\dot{\rho} = -i(H_{\text{NH}}\rho - \rho H_{\text{NH}}^\dagger), \quad (20)$$

where the non-Hermitian Hamiltonian reads

$$H_{\text{NH}} = H - \frac{i}{2}(\Gamma_1 A_{be}^\dagger A_{be} + \Gamma_2 A_{eb}^\dagger A_{eb} + \sum_j \gamma_j^{(0)} A_{jj}^\dagger A_{jj}). \quad (21)$$

The NHH method is valid as long as the dissipation and dephasing rates Γ_j and $\gamma_j^{(0)}$ are much smaller than the typical frequency of the Hamiltonian.

By the NHH method, the final state of the system in the interaction picture is written as

$$\begin{aligned} |\psi(t_3, t_2, t_1)\rangle &= U_f^I(t_1 + t_2 + t_3 + \delta t_a + \delta t_b + \delta t_c, \\ &t_1 + t_2 + \delta t_a + \delta t_b + \delta t_c) \\ &\times U_p^I(t_1 + t_2 + \delta t_a + \delta t_b + \delta t_c, t_1 + t_2 + \delta t_a + \delta t_b) \\ &\times U_f^I(t_1 + t_2 + \delta t_a + \delta t_b, t_1 + \delta t_a + \delta t_b) \\ &\times U_p^I(t_1 + \delta t_a + \delta t_b, \tau + \delta t_a) U_f^I(t_1 + \delta t_a, \delta t_a) \\ &\times U_p^I(\delta t_a, 0) |\psi(0)\rangle, \end{aligned} \quad (22)$$

where U_p^I (U_f^I) represents the evolution operator with (without) the probe pulses included in the interaction picture. We consider that the probe pulses are so strong and their durations are so short that both the dissipation and dephasing during the excitations can be neglected. In the interaction picture, the Hamiltonians during probe pulses are explicitly written as

$$H_p^I = -\frac{1}{2}\Omega_{be}e^{-i\vec{k}_p\cdot\vec{r}}|b\rangle\langle e| + \text{h.c.}, \quad (23)$$

while the Hamiltonians during the free evolutions read

$$H_f^I = -\frac{1}{2}\Omega_{ec}(|e\rangle\langle c| + |c\rangle\langle e|) - \frac{i}{2}(\Gamma_1|e\rangle\langle e| + \Gamma_2|b\rangle\langle b| + \sum_j \gamma_j^{(0)}|j\rangle\langle j|). \quad (24)$$

Hereinto, we approximate the probe pulses as square pulses. The time evolutions under H_f^I for initial states $|b\rangle$, $|e\rangle$ and $|c\rangle$ are respectively written as

$$U_f^I(t_c)|b\rangle = C_{bb}(t_c)|b\rangle, \quad (25)$$

$$U_f^I(t_c)|e\rangle = C_{ee}(t_c)|e\rangle + C_{ce}(t_c)|c\rangle, \quad (26)$$

$$U_f^I(t_c)|c\rangle = C_{ec}(t_c)|e\rangle + C_{cc}(t_c)|c\rangle, \quad (27)$$

where t_c ($c = 1, 2, 3$) are time intervals, and

$$C_{bb}(t) = e^{-\frac{1}{2}\gamma_b t}, \quad (28)$$

$$C_{ee}(t) = e^{-\frac{1}{2}\gamma_{ec}^+ t} \frac{(2i\tilde{\Omega}_- - \gamma_{ec}^-)e^{\frac{i}{2}\tilde{\Omega}_- t} + (2i\tilde{\Omega}_- + \gamma_{ec}^-)e^{-\frac{i}{2}\tilde{\Omega}_- t}}{4i\tilde{\Omega}_-} \quad (29)$$

$$C_{ce}(t) = e^{-\frac{1}{2}\gamma_{ec}^+ t} \frac{\Omega_{ec} \left(e^{i\tilde{\Omega}_- t} - 1 \right) e^{-\frac{i}{2}\tilde{\Omega}_- t}}{2\tilde{\Omega}_-}, \quad (30)$$

$$C_{ec}(t) = e^{-\frac{1}{2}\gamma_{ec}^+ t} \frac{\Omega_{ec} \left(e^{i\tilde{\Omega}_- t} - 1 \right) e^{-\frac{i}{2}\tilde{\Omega}_- t}}{2\tilde{\Omega}_-}, \quad (31)$$

$$C_{cc}(t) = e^{-\frac{1}{2}\gamma_{ec}^+ t} \frac{(2i\tilde{\Omega}_- - \gamma_{ec}^-)e^{-\frac{i}{2}\tilde{\Omega}_- t} + (2i\tilde{\Omega}_- + \gamma_{ec}^-)e^{\frac{i}{2}\tilde{\Omega}_- t}}{4i\tilde{\Omega}_-}. \quad (32)$$

In the subscript of $C_{ji}(t)$, i and j represent the initial and final state during the evolution,

and

$$\gamma_b = \Gamma_2 + \gamma_b^{(0)}, \quad (33)$$

$$\gamma_{ec}^- = \Gamma_1 + \gamma_e^{(0)} - \gamma_c^{(0)}, \quad (34)$$

$$\tilde{\Omega}_- = \sqrt{\Omega_{ec}^2 - \frac{1}{4}(\gamma_{ec}^-)^2}. \quad (35)$$

Meanwhile, the time evolutions under H_p^I for three initial states are respectively written as

$$U_p^I(\delta t_p)|b\rangle = N_p \left(|b\rangle + \beta_p e^{i\vec{k}_p \vec{r}} |e\rangle \right), \quad (36)$$

$$U_p^I(\delta t_p)|e\rangle = N_p \left(\beta_p e^{-i\vec{k}_p \vec{r}} |b\rangle + |e\rangle \right), \quad (37)$$

$$U_p^I(\delta t_p)|c\rangle = |c\rangle, \quad (38)$$

where $\beta_p = i\Omega_{be}\delta t_p/2$, and the normalization constants are

$$N_p = (1 + |\beta_p|^2)^{-1/2},$$

with δt_p ($p = a, b, c$) being time intervals of the probe pulses.

Straightforward, the final density matrix reads $\rho(t) = |\psi(t_3, t_2, t_1)\rangle\langle\psi(t_3, t_2, t_1)|$. Under the situation that the spacing of the energy levels are much wider than their linewidths, its non-diagonal elements ρ_{eb} and ρ_{be} emit signals near ω_e in the frequency domain, which are proportional to the polarization

$$\vec{P}_{eb}(t_3, t_2, t_1) = \rho_{eb}(t_3, t_2, t_1)\vec{\mu}_{be} + \text{c.c.} \quad (39)$$

Here, $\vec{\mu}_{be}$ is the transition electric dipole between $|e\rangle$ and $|b\rangle$. On account of the phase-matching condition, the polarization $\vec{P}_{\text{RP}}(t_3, t_2, t_1)$ in the RP direction along $\vec{k}_s = -\vec{k}_a + \vec{k}_b + \vec{k}_c$ is selected. Furthermore, by double Fourier transforms with respect to t_1 and t_3 , the RP

signal of the 2DS reads

$$\vec{P}_{\text{RP}}(\omega_3, t_2, \omega_1) = \mathcal{F} \left[\vec{P}_{\text{RP}}(t_3, t_2, t_1) \right], \quad (40)$$

and is explicitly written as

$$\begin{aligned} \vec{P}_{\text{RP}}(\omega_3, t_2, \omega_1) = & e^{-i\omega_e t_f} N_a^2 N_b N_c \beta_a^* \times \\ & [N_b N_c \beta_b^* \beta_c \tilde{G}_{bebe}(\omega_1) G_{bbbb}(t_2) \tilde{G}_{ebeb}(\omega_3) \\ & + N_b N_c \beta_b \beta_c^* \tilde{G}_{bebe}(\omega_1) G_{eeee}(t_2) \tilde{G}_{ebeb}(\omega_3) \\ & + N_b \beta_b \beta_c^* \tilde{G}_{bebe}(\omega_1) G_{ceee}(t_2) \tilde{G}_{ebcb}(\omega_3) \\ & + N_c \beta_b \beta_c^* \tilde{G}_{bcbe}(\omega_1) G_{eeec}(t_2) \tilde{G}_{ebeb}(\omega_3) \\ & + \beta_b \beta_c^* \tilde{G}_{bcbe}(\omega_1) G_{ceec}(t_2) \tilde{G}_{ebcb}(\omega_3)]. \end{aligned} \quad (41)$$

Here, $t_f = \sum_p \delta t_p$, and $\exp(-i\omega_e t_c)$ are absorbed into $G_{ijkl}(t)$ and $\tilde{G}_{ijkl}(\omega)$. The quasi-Green functions and their Fourier transform for the NHH method are written as

$$G_{ijkl}(t) = C_{jl}^*(t) C_{ik}(t) e^{-i\omega_e t}, \quad (42)$$

$$\tilde{G}_{ijkl}(\omega) = \mathcal{F} [G_{ijkl}(t)], \quad (43)$$

where kl represent the initial density matrix element $|k\rangle\langle l|$ before an evolution, and ij represent the final density matrix element $|i\rangle\langle j|$ after the evolution. Since C_{ji} (C_{ji}^*) are components of the ket (bra), we rearrange the subscripts of $C_{jl}^* C_{ik}$ as G_{ijkl} analogue to those of the Green

functions. After the Fourier transform, the quasi-Green functions read

$$\tilde{G}_{bebe}(\omega) = \frac{-\gamma_{ec}^- + 2[\gamma_b + \gamma_{ec}^+ + 2i(\omega - \omega_e)]}{\tilde{\Omega}_-^2 + [\gamma_b + \gamma_{ec}^+ + 2i(\omega - \omega_e)]^2}, \quad (44)$$

$$\tilde{G}_{bcbe}(\omega) = \frac{2i\Omega_{ec}}{\tilde{\Omega}_-^2 + [\gamma_b + \gamma_{ec}^+ + 2i(\omega - \omega_e)]^2}, \quad (45)$$

$$\tilde{G}_{ebeb}(\omega) = \frac{-\gamma_{ec}^- + 2[\gamma_b + \gamma_{ec}^+ - 2i(\omega - \omega_e)]}{\tilde{\Omega}_-^2 + [\gamma_b + \gamma_{ec}^+ - 2i(\omega - \omega_e)]^2}, \quad (46)$$

$$\tilde{G}_{ebcb}(\omega) = \frac{2i\Omega_{ec}}{\tilde{\Omega}_-^2 + [\gamma_b + \gamma_{ec}^+ - 2i(\omega - \omega_e)]^2}. \quad (47)$$

The Feynman diagrams of each term in Eq. (41) are shown in Fig. 3, with (a)-(e) corresponding to the five terms in turn. The initial and final states of evolutions during t_1 , t_2 and t_3 are explicitly given. Compared with Fig. 2, two of the five Liouville paths are the same, i.e., Fig. 3(a) vs Fig. 2(d) and Fig. 3(b) vs Fig. 2(a). Meanwhile, the other two Liouville paths disappear, i.e., Fig. 2(b) and (c), and three new Liouville paths emerge, i.e., Fig. 3(c)-(e). More specifically, Fig. 3(c) remains the same as Fig. 2(a) until the initial state of the t_2 evolution, and diverges at the final state of it. In addition, Fig. 3(d) and (e) are different from Fig. 2 at the final state of the t_1 evolution. We note that it is these distinctions that lead to the difference between the two methods.

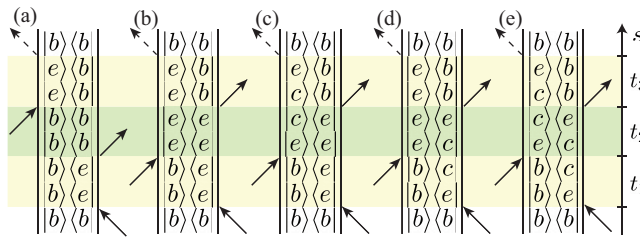


Figure 3: Feynman diagrams of the three-level system by the NHH method. (a)-(e) demonstrate the five Liouville paths of the RP signal, i.e., the five terms in Eq. (41). The evolution during t_2 is highlighted by green, and the evolutions during t_1 and t_3 are marked by yellow.

Results and Discussion

In this section, we compare the 2DS by the two methods with the same parameters, i.e., the ground-state energy $\omega_b = 0$, the excited-state energy $\omega_e/2\pi = 4.33$ THz, and the metastable-state energy $\omega_c/2\pi = 1$ MHz.^{45–47} The Rabi frequencies and durations of the probe pulses are $\Omega_{be}/2\pi = 50$ MHz and $\delta t_p = 0.5$ ns, with a bandwidth of $2\pi \times 1.8$ GHz, while the Rabi frequency of the control field is $\Omega_{ec} = 2$ MHz.⁴⁸ The dissipation rates are $\Gamma_1/2\pi = 1$ kHz and $\Gamma_2/2\pi = 0.03$ kHz, and the pure-dephasing rates of all states are homogeneously $\gamma_b^{(0)}/2\pi = \gamma_e^{(0)}/2\pi = \gamma_c^{(0)}/2\pi = 0.1$ MHz.^{49,50}

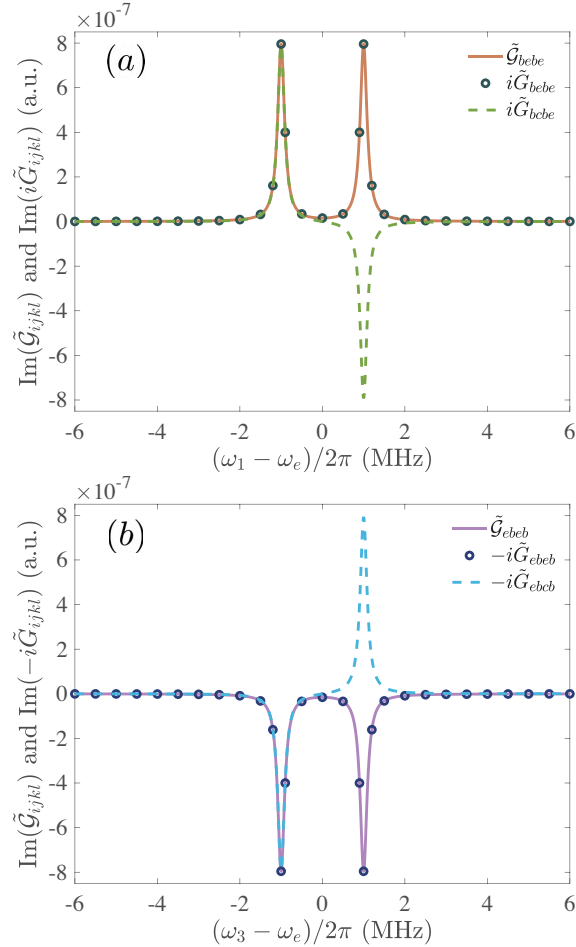


Figure 4: Comparison of the Green functions by the RF (\tilde{G}_{ijkl}) and the NHH (\tilde{G}_{ijkl}) approaches. (a) \tilde{G}_{bebe} vs $i\tilde{G}_{bebe}$, and $i\tilde{G}_{bebe}$ are respectively denoted by the orange solid, dark-green circles, light-green dash lines, (b) \tilde{G}_{ebeb} vs $-i\tilde{G}_{ebeb}$, and $-i\tilde{G}_{ebeb}$ are respectively denoted by the purple solid, dark-blue circles, light-blue dash lines.

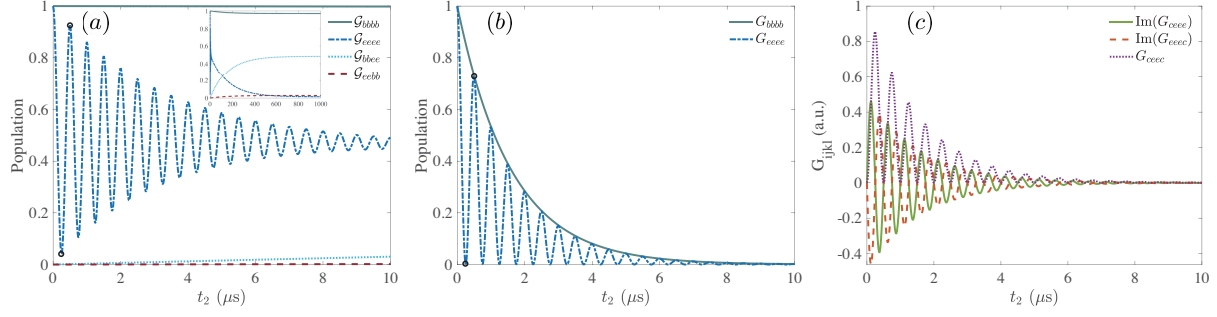


Figure 5: Population dynamics by (a) the RF formalism, (b) the NHH method and (c) the Green function $G_{ijkl}(t)$ for the coherences vs time. The dark-green solid and dark-blue dash-dotted lines denote \mathcal{G}_{bbbb} (G_{bbbb}) and \mathcal{G}_{eeee} (G_{eeee}), respectively. The light-blue dotted and dark-red dashed lines respectively denote \mathcal{G}_{bbec} and \mathcal{G}_{eebb} , while the light-green solid, orange dashed, and purple dotted lines respectively denote $\text{Im}(G_{ceee})$, $\text{Im}(G_{eeec})$ and G_{ceec} . Here, G_{ceee} and G_{eeec} are purely imaginary. The inset in (a) shows the long-time regime, and the black circles in the first two subfigures label $t_2 = 0.24 \mu\text{s}$ and $t_2 = 0.50 \mu\text{s}$, respectively.

The comparison between the Green function $\tilde{\mathcal{G}}_{ijkl}(\omega)$ and the quasi-Green functions $\tilde{G}_{ijkl}(\omega)$ are shown in Fig. 4. The additional factors $\pm i$ before $\tilde{G}_{ijkl}(\omega)$ are included due to the different definitions of the Fourier transforms in the RF and the NHH approaches.²⁹ The curves of $\text{Im}(\tilde{\mathcal{G}}_{bebe})$ and $\text{Im}(i\tilde{\mathcal{G}}_{bebe})$ are identical, and so are $\text{Im}(\tilde{\mathcal{G}}_{ebcb})$ and $\text{Im}(-i\tilde{\mathcal{G}}_{ebcb})$. Concurrently, the curve of $\text{Im}(i\tilde{\mathcal{G}}_{bcbe})$ coincides with $\text{Im}(\tilde{\mathcal{G}}_{bebe})$ and $\text{Im}(i\tilde{\mathcal{G}}_{bebe})$ when $\omega - \omega_e < 0$, and differs from them by a sign when $\omega - \omega_e > 0$. The same behavior can be observed in the curves of $\text{Im}(-i\tilde{\mathcal{G}}_{ebcb})$ vs $\text{Im}(\tilde{\mathcal{G}}_{ebcb})$ and $\text{Im}(-i\tilde{\mathcal{G}}_{ebcb})$. The imaginary parts of the Green functions for ω_1 dominate the absorption of probe pulses, with higher positive values representing greater absorption and lower negative values representing more emission. The opposite sign of the imaginary parts of the Green functions for ω_3 have the same influence. The control field causes the original absorption peak at ω_e to be split into two peaks with approximately-symmetrical locations around ω_e , just as EIT happens. Furthermore, the emergent evolution paths of $\tilde{\mathcal{G}}_{bcbe}$ and $\tilde{\mathcal{G}}_{ebcb}$ introduce emission peaks. Consequently, the splitting determines the location of peaks on 2DS, and the influence of the emission peaks will be discussed later.

The population dynamics vs the population time t_2 by the RF formalism and the NHH method are compared in Fig. 5, with only possible Liouville paths demonstrated. Figure 5(a)

illustrates the population dynamics by the RF formalism in the subspace spanned by $|b\rangle$ and $|e\rangle$. Figure 5(b) depicts the dynamics of the diagonal elements $|b\rangle\langle b|$ and $|e\rangle\langle e|$ of the density matrix by the NHH method. Figure 5(c) shows the quasi-Green functions for the three Liouville paths by the NHH method in addition to the RF formalism. Notice that although the initial (final) state of G_{ceee} (G_{eecc}) is the population state, its final (initial) state is a coherent state. This sharp contrasts yield purely-imaginary quasi-Green functions.

The dynamic processes of \mathcal{G}_{bbbb} and G_{bbbb} exhibit a damping with different timescales for reaching the steady states, i.e., $(\Gamma_1 + \Gamma_2)^{-1}$ vs $(\gamma_b/2)^{-1}$. For \mathcal{G}_{eeee} , G_{eeee} and G_{ceec} , there are coherent oscillations due to the coherent population transfer. The oscillation frequency of \mathcal{G}_{eeee} is $\tilde{\Omega}_+$ when $\Omega_{ec} > \gamma_{ec}^+/2$. Meanwhile, the oscillation frequencies of G_{eeee} and G_{ceec} are identical, i.e., $\tilde{\Omega}_-$ when $\Omega_{ec} > \gamma_{ec}^-/2$. These three curves all oscillate at the same frequency, since $\tilde{\Omega}_+ \approx \tilde{\Omega}_- \approx \Omega_{ec}$ when $\Omega_{ec} \gg \gamma_{ec}^\pm$. On the other hand, oscillations undergo damping with a time scale of $1/\gamma_{ec}^+$, and ultimately disappear due to dephasing and dissipation.

There is a phase shift of π between the oscillations of G_{eeee} and G_{ceec} . When $G_{eeee} = 0$, G_{ceec} reaches its maximum values, indicating that the maximum population transfer corresponds to the maximum coherence. In addition, the imaginary parts of G_{ceee} and G_{eecc} exhibit inverse-synchronized damping oscillations. They oscillate around zero, with a phase shift of π between them as well. However, they have no direct effect on the final 2DS. Moreover, although the oscillation behaviors by the two methods exhibit similarity, they tend to reach different steady states in long-time limit, e.g., $\Gamma_1/(\Gamma_1 + \Gamma_2)$ for \mathcal{G}_{bbbb} vs zero for G_{bbbb} , according to Eqs. (19) and (28). This remarkable discrepancy is due to the fact that the Hamiltonian in the NHH method is not Hermitian, i.e., $H^\dagger \neq H$, so the conservation of the trace is violated and thus the detailed balance breaks down.

To illustrate this more clearly, we present a comparison of the trace dynamics during t_2 for the two methods in Fig. 6, where the orange circles and dashed lines always remain at unity, while the dark-blue circles and dashed lines decay exponentially. The circles (dashed lines) represent the summation of all populations evolving initially from the energy level b

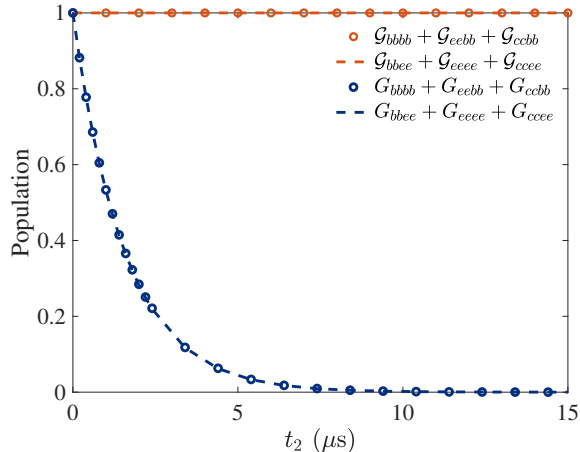


Figure 6: Conservation of trace for different initial states by the RF and the NHH approaches. The orange circles and dashed lines denote the traces of the RF formalism starting from the initial states $|b\rangle$ and $|e\rangle$, and the dark-blue circles and dashed lines denote the traces of the NHH method starting from the initial states $|b\rangle$ and $|e\rangle$, respectively.

(e). The result indicates that the trace is conserved for the RF formalism no matter how long the system evolves. In contrast, the trace is not conserved for the NHH method whatever the system in t_2 is initially prepared.

For further comparison of the two approaches, representative points are selected according to their population dynamics, i.e., $t_2 = 0, 0.24, 0.5, 10^3 \mu\text{s}$, and the 2DS for each method at these population times are plotted in Fig. 7 (a) through (h). The first three t_2 values correspond to the initial state, the first valley and the first peak of the population dynamics, respectively, for both the RF formalism and the NHH method. The last t_2 is selected for observing results at the steady state. In both methods, the introduction of the control field results in splitting of the homogeneously-broadened peak into four smaller peaks on 2DS.⁴⁴ The RF formalism and the NHH method, exhibiting identical peak positions, indicate that the spacings between peaks are identical. These spacings between the adjacent diagonal and non-diagonal peaks equal to $2.005 \times 2\pi$ MHz, which are approximately the splitting width $2 \times 2\pi$ MHz of the Green functions according to Fig. 4.

The RP signals of the two methods are respectively normalized by their maximum values at $t_2 = 0 \mu\text{s}$, thereby obtaining relative signals for the sake of simplicity. At $t_2 = 0 \mu\text{s}$, 2DS

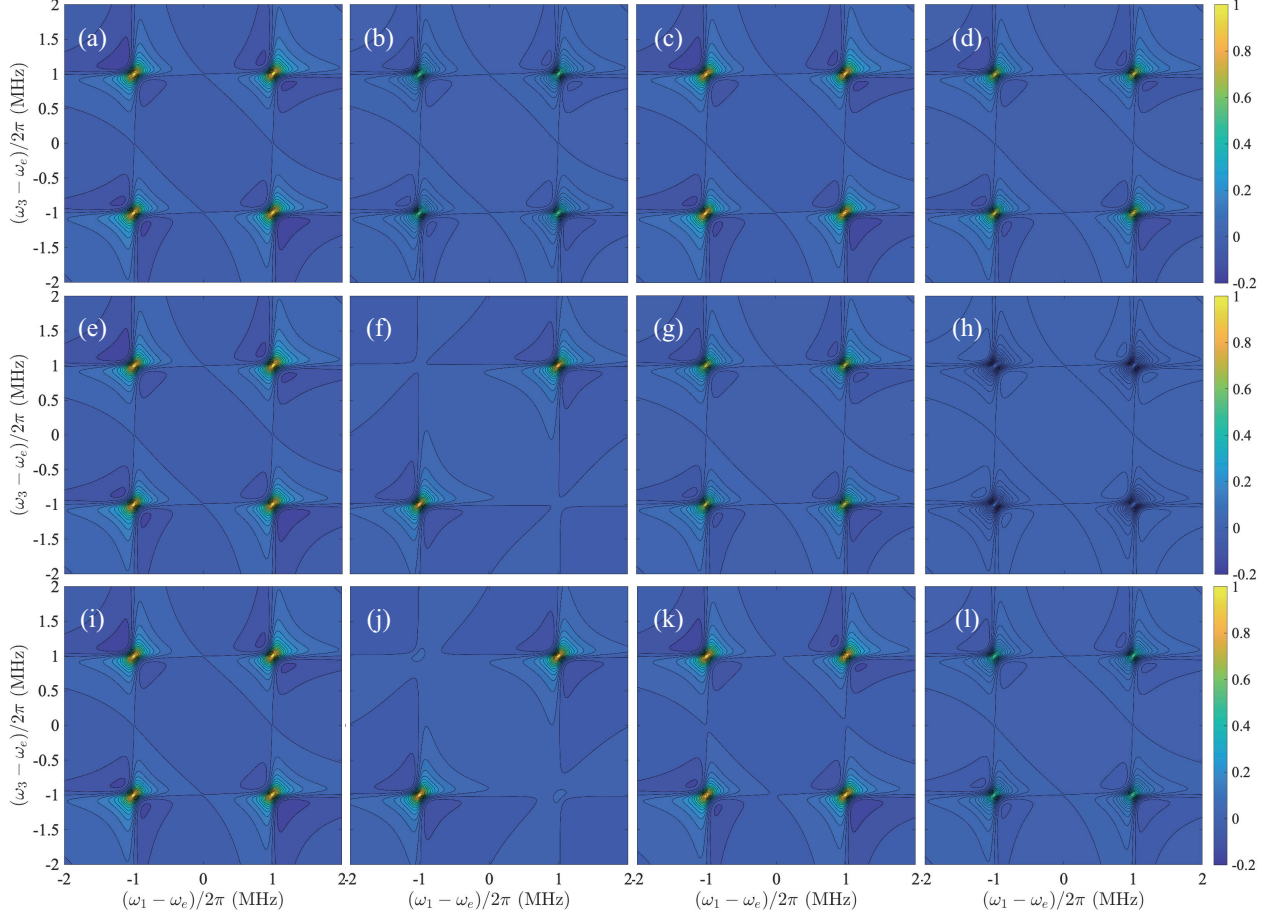


Figure 7: Comparison of the 2DS for the two methods. The first (second) row correspond to the RF formalism (the NHH method). The third row is by the RF formalism with Liouville paths of the same as the NHH method in Fig. 3. The 2DS are plotted when (a,e,i) $t_2 = 0 \mu s$, (b,f,j) $t_2 = 0.24 \mu s$, (c,g,k) $t_2 = 0.50 \mu s$, (d,h,l) $t_2 = 10^3 \mu s$.

of the two methods are close to each other. Both methods yield the highest four peaks, the relative heights of one peak and its counterpart from the other method are approximately identical, with a variance at the scale of 10^{-4} . At $t_2 = 10^3 \mu s$, the peaks of the RF formalism retain their scale because the trace is conserved. The peaks of the NHH method, however, undergo an overall attenuation as t_2 increases, since its trace is not conserved. The peak heights rapidly attenuate in the first few seconds, and are of the order of 10^{-273} different from the initial state at $t_2 = 10^3 \mu s$.

The four peaks of the RF formalism synchronously become lower at $t_2 = 0.24 \mu s$, then raise at $t_2 = 0.5 \mu s$. They exhibit synchronous oscillating behavior, which is dominated by

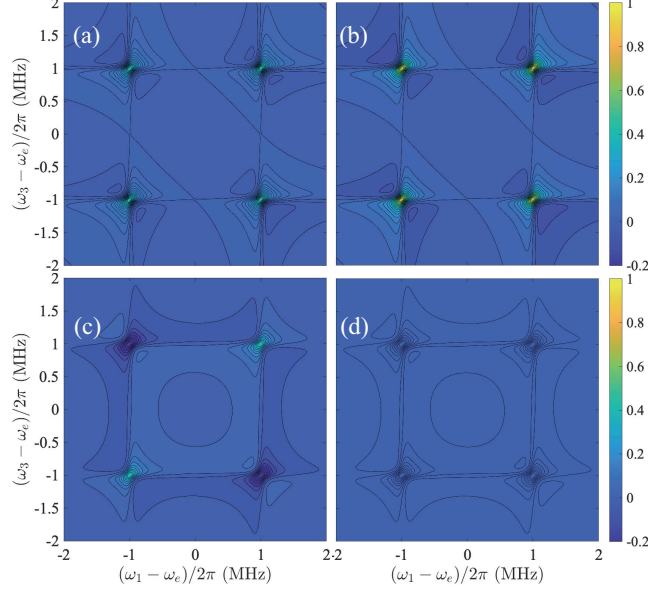


Figure 8: Comparison of the NHH method's partial 2DS with different evolving paths in t_1 and t_3 . The first (second) row correspond to the summation of the paths evolving from $|b\rangle\langle e|$ to $|b\rangle\langle e|$ ($|b\rangle\langle e|$ to $|b\rangle\langle c|$) in t_1 , while evolving from $|e\rangle\langle b|$ to $|e\rangle\langle b|$ ($|c\rangle\langle b|$ to $|e\rangle\langle b|$) in t_3 . The 2DS are plotted when (a,c) $t_2 = 0.24 \mu\text{s}$, (b,d) $t_2 = 0.50 \mu\text{s}$.

\mathcal{G}_{eeee} . The NHH method, on the other hand, has little variance on the diagonal peaks despite attenuation, while the non-diagonal peaks continue to oscillate. According to the Liouville paths of each term in t_1 and t_3 , the RP signal of the NHH method is divided into three parts. The paths of Fig. 3(a) and (b) are added together as the part that experiences $|b\rangle\langle e|$ evolving to $|b\rangle\langle e|$ during t_1 , while $|e\rangle\langle b|$ evolving to $|e\rangle\langle b|$ during t_3 . Figure 3(c) and (d) are added together and have little effect on the final 2DS. Figure 3(e) is classified into a separate part for it experiences time evolution from $|b\rangle\langle e|$ to $|b\rangle\langle c|$ in t_1 and $|c\rangle\langle b|$ to $|e\rangle\langle b|$ in t_3 . The 2DS of the first and the third parts are demonstrated in Fig. 8. In Fig. 8(c), the non-diagonal peaks are negative, which are caused by the emission peaks of the quasi-Green function in Fig. 4. The remaining positive peaks at $t_2 = 0.24 \mu\text{s}$ are shallow, but are summed up to be the same scale in accordance with the peak heights at $t_2 = 0 \mu\text{s}$. At $t_2 = 0.50 \mu\text{s}$, on the other hand, Fig. 8(d) gives little contribution and the final 2DS is dominated by Fig. 8(b). As a result, Fig. 8(b) is almost the same as Fig. 7(g). These 2DS are consistent with the population dynamics. In other words, having less population on the excited state $|e\rangle$ despite

decay is the feature of stronger coherence between the energy levels e and c , as well as more contribution from the Liouville path Fig. 3(e).

Finally, for a better comparison of the two approaches, we recalculate the 2DS by the RF formalism with Liouville paths the same as the NHH method in Fig. 3. The RP signal is written as

$$\begin{aligned}
S_{\text{RP}}^{(3)}(\omega_3, t_2, \omega_1) = & \tilde{\mathcal{G}}_{ebeb}(\omega_3)\mathcal{G}_{bbbb}(t_2)\tilde{\mathcal{G}}_{bebe}(\omega_1) \\
& + \tilde{\mathcal{G}}_{ebeb}(\omega_3)\mathcal{G}_{eeee}(t_2)\tilde{\mathcal{G}}_{bebe}(\omega_1) \\
& + \tilde{\mathcal{G}}_{ebcb}(\omega_3)\mathcal{G}_{ceee}(t_2)\tilde{\mathcal{G}}_{bebe}(\omega_1) \\
& + \tilde{\mathcal{G}}_{ebeb}(\omega_3)\mathcal{G}_{eeec}(t_2)\tilde{\mathcal{G}}_{bcbe}(\omega_1) \\
& + \tilde{\mathcal{G}}_{ebcb}(\omega_3)\mathcal{G}_{ceec}(t_2)\tilde{\mathcal{G}}_{bcbe}(\omega_1).
\end{aligned} \tag{48}$$

Correspondingly, the additional Green functions are written as

$$\tilde{\mathcal{G}}_{bcbe}(\omega_1) = \frac{2\Omega_{ec}}{4(\omega_1 - \omega_{cb} - i\gamma_{bc})(-\omega_1 + \omega_{cb} + i\gamma_{eb}) + \Omega_{ec}^2}, \tag{49}$$

$$\tilde{\mathcal{G}}_{ebcb}(\omega_3) = \frac{2\Omega_{ec}}{4(\omega_3 - \omega_{eb} + i\gamma_{bc})(-\omega_3 + \omega_{eb} - i\gamma_{eb}) + \Omega_{ec}^2}, \tag{50}$$

$$\mathcal{G}_{ceee}(t_2) = \frac{\Omega_{ec}}{4\tilde{\Omega}_+} \left(-1 + e^{2i\tilde{\Omega}_+ t} \right) e^{-\frac{1}{2}(\gamma_{ec}^+ + 2i\tilde{\Omega}_+)t}, \tag{51}$$

$$\mathcal{G}_{eeec}(t_2) = -\mathcal{G}_{ceee}(t_2), \tag{52}$$

$$\begin{aligned}
\mathcal{G}_{ceec}(t_2) = & \frac{\gamma_{ec}^+ \sin(\tilde{\Omega}_+ t) - 2\tilde{\Omega}_+ \cos(\tilde{\Omega}_+ t)}{4\tilde{\Omega}_+} e^{-\frac{1}{2}\gamma_{ec}^+ t} \\
& + \frac{1}{2} e^{-\gamma_{ec}^+ t},
\end{aligned} \tag{53}$$

and the 2DS are demonstrated in Fig. 7 (i) through (l). It is shown that when the RF formalism and the NHH method are applied using the same Liouville paths, the resulting 2DS exhibit quite similar behaviors. The only discrepancy of the 2DS occurs significantly in the long-time limit, where the peak heights by the NHH method markedly decrease as compared to the counterparts by the RF formalism. These results reveal that the two

methods are mostly consistent when having the identical Liouville paths.

Considering that the Liouville paths of the RF formalism in Fig. 2 do not include terms like $|b\rangle\langle c|$ or $|e\rangle\langle c|$ which are induced by the control field, we believe that the original RF formalism fails in accurately describing the time evolutions of the system and identifying all relevant Liouville paths. Conversely, the NHH method, enhanced by our simple improvement with the quasi-Green function, effectively provides the appropriate Liouville paths.

Conclusion

In this paper, we compare the NHH method and the RF formalism with their advantages and disadvantages in the obtaining of 2DS. In particular, we give a simple simplification to the computation processes of the NHH method by introducing the quasi-Green function, which improves its interpretive capacity. Both methods are demonstrated by gaining the RP signal of 2DS for the three-level system under the influence of a control field. The NHH signal is decomposed into the sum of the products, of which three quasi-Green functions corresponding to different t_c are multiplied. An intuitive explanation of the NHH method is thus given directly in terms of the Feynman diagrams. It is worth noting that the NHH method yields signal with more Liouville paths and evolution information. We compare the population dynamics of the two methods in t_2 , obtaining similar oscillatory behavior in the first few periods, but different steady states for the long-time evolution. The comparison of the sum of populations on the three levels in t_2 indicates that for the RF formalism the probability is conserved, while for the NHH method the probability keeps decaying. This decay leads to the different steady states in the population dynamics, and also to a weakening of the emitted signal as t_2 increases. To sum up, although the NHH method suffers from the limitation of non-conservative population, it is particularly suitable for investigating dissipative or complex systems. Besides, the equation-of-motion method, which has a conserved population but an even higher computational complexity, may help in this

scene.⁵¹

We plot the 2DS for four representative t_2 's. Both methods yield splitting peaks with the same locations for each split peak. For the RF formalism, the heights of the four peaks oscillate synchronously. In contrast, for the NHH method, the four peaks oscillate for a few periods with continuous attenuation, and the oscillation amplitude of the non-diagonal peaks are more significant than that of the diagonal peaks. We show that the disappearance and emergence of off-diagonal peaks in 2DS by the NHH approach are attributed to the interference of different Feynman diagrams induced by the control fields. Furthermore, by comparing the 2DS of the two methods with the same Liouville paths, we show that the main difference between the two approaches is due to the introduction of some additional Feynman diagrams and the disappearance of some less-important Feynman diagrams induced by the control fields.

Overall, the differences between the 2DS of the two methods are attributed to the fact that in the NHH method there are unidirectional population losses to the environment, and there are more abundant Liouville paths. The NHH method has its advantage of obtaining the signals directly from the time evolution, and thus is less likely to omit any possible Liouville paths. This approach can be more applicable in complicated systems with complex energy structure and transition paths, as compared to the RF formalism. It will help to obtain 2DS more comprehensively and has prospects for exploring the dynamics of molecular or atomic systems with complex protocols.

Acknowledgement

We thank Lipeng Chen for valuable comments on the paper. This work is supported by Innovation Program for Quantum Science and Technology under grant No. 2023ZD0300200, the Natural Science Foundation of Beijing Municipality under Grant No. 1202017 and the National Natural Science Foundation of China under Grant Nos. 11674033, 11505007, and

References

- (1) Mukamel, S. Multidimensional Femtosecond Correlation Spectroscopies of Electronic and Vibrational Excitations. *Annu. Rev. Phys. Chem.* **2000**, *51*, 691.
- (2) Fuller, F. D.; Ogilvie, J. P. Experimental Implementations of Two-Dimensional Fourier Transform Electronic Spectroscopy. *Annu. Rev. Phys. Chem.* **2015**, *66*, 667–690.
- (3) Gelzinis, A.; Augulis, R.; Butkus, V.; Robert, B.; Valkunas, L. Two-Dimensional Spectroscopy for Non-Specialists. *Biochim. Biophys. Acta. Bioenerg.* **2019**, *1860*, 271–285.
- (4) Sun, Z.-H.; Yao, Y.-X.; Ai, Q.; Cheng, Y.-C. Theory of Center-Line Slope in 2D Electronic Spectroscopy with Static Disorder. *Adv. Quantum Tech.* **2023**, *6*, 2300163.
- (5) Tseng, C.-H.; Matsika, S.; Weinacht, T. C. Two-Dimensional Ultrafast Fourier Transform Spectroscopy in the Deep Ultraviolet. *Opt. Express* **2009**, *17*, 18788–18793.
- (6) Westenhoff, S.; Palecek, D.; Edlund, P.; Smith, P.; Zigniantas, D. Coherent Picosecond Exciton Dynamics in a Photosynthetic Reaction Center. *J. Am. Chem. Soc.* **2012**, *134*, 16484–16487.
- (7) Rosenfeld, D. E.; Gengeliczki, Z.; Smith, B. J.; Stack, T. D. P.; Fayer, M. D. Structural Dynamics of a Catalytic Monolayer Probed by Ultrafast 2D IR Vibrational Echoes. *Science* **2011**, *334*, 634–639.
- (8) Woerner, M.; Kuehn, W.; Bowlan, P.; Reimann, K.; Elsaesser, T. Ultrafast Two-Dimensional Terahertz Spectroscopy of Elementary Excitations in Solids. *New J. Phys.* **2013**, *15*, 025039.
- (9) Lu, J.; Li, X.; Zhang, Y.; Hwang, H. Y.; Ofori-Okai, B. K.; Nelson, K. A. Two-Dimensional Spectroscopy at Terahertz Frequencies. *Top. Curr. Chem.* **2018**, *376*, 6.

- (10) Lewis, K.; Ogilvie, J. P. Probing Photosynthetic Energy and Charge Transfer with Two-Dimensional Electronic Spectroscopy. *J. Phys. Chem. Lett.* **2012**, *3*, 503–510.
- (11) Mehlenbacher, R. D.; Wang, J. L.; Kearns, N. M.; Shea, M. J.; Flach, J. T.; McDonough, T. J.; Wu, M.-Y.; Zanni, M. T. Ultrafast Exciton Hopping Observed in Bare Semiconducting Carbon Nanotube Thin Films with Two-Dimensional White-Light Spectroscopy. *J. Phys. Chem. Lett.* **2016**, *7*, 2024–2031.
- (12) Branczyk, A. M.; Turner, D. B.; Scholes, G. D. Crossing Disciplines - A View on Two-Dimensional Optical Spectroscopy. *Ann. Phys. (N.Y.)* **2014**, *526*, 31–49.
- (13) Rubtsova, N. I.; Rubtsov, I. V. Vibrational Energy Transport in Molecules Studied by Relaxation-Assisted Two-Dimensional Infrared Spectroscopy. *Annu. Rev. Phys. Chem.* **2015**, *66*, 717–738.
- (14) Golonzka, O.; Khalil, M.; Demirdöven, N.; Tokmakoff, A. Vibrational Anharmonicities Revealed by Coherent Two-Dimensional Infrared Spectroscopy. *Phys. Rev. Lett.* **2001**, *86*, 2154–2157.
- (15) Butkus, V.; Valkūnas, L.; Abramavičius, D. Molecular Vibrations-Induced Quantum Beats in Two-Dimensional Electronic Spectroscopy. *J. Chem. Phys.* **2012**, *137*, 044513.
- (16) Milota, F.; Sperling, J.; Nemeth, A.; Mancal, T.; Kauffmann, H. F. Two-Dimensional Electronic Spectroscopy of Molecular Excitons. *Acc. Chem. Res.* **2009**, *42*, 1364–1374.
- (17) Nagahara, T.; Camargo, F. V. A.; Xu, F. G.; Ganzer, L.; Russo, M.; Zhang, P. F.; Perri, A.; Valbuena, G. C.; Heisler, I. A.; D’Andrea, C.; Polli, D.; Müllen, K.; Feng, X. L.; Mai, Y. Y.; Cerullo, G. Electronic Structure of Isolated Graphene Nanoribbons in Solution Revealed by Two-Dimensional Electronic Spectroscopy. *Nano Lett.* **2024**, *24*, 797–804.

- (18) Krecik, M.; Hein, S. M.; Schoth, M.; Richter, M. Detection of Dark-State Relaxation through Two-Dimensional Nano-Optical Spectroscopy. *Proc. SPIE* **2015**, *9361*, 936109.
- (19) Jansen, T. L. C.; Knoester, J. Calculation of Two-Dimensional Infrared Spectra of Ultrafast Chemical Exchange with Numerical Langevin Simulations. *J. Chem. Phys.* **2007**, *127*, 234502.
- (20) Herrera, A.; Fernandez-Valle, E.; Martinez-Alvarez, R.; Molero, D.; Pardo, Z. D.; Sáez, E.; Gal, M. Real-Time Monitoring of Organic Reactions with Two-Dimensional Ultrafast TOCSY NMR Spectroscopy. *Angew. Chem. Int. Ed.* **2009**, *48*, 6274–6277.
- (21) Ghosh, A.; Ostrander, J. S.; Zanni, M. T. Watching Proteins Wiggle: Mapping Structures with Two Dimensional Infrared Spectroscopy. *Chem. Rev.* **2017**, *117*, 10726–10759.
- (22) Maiti, K. S. Two-Dimensional Infrared Spectroscopy Reveals Better Insights of Structure and Dynamics of Protein. *Molecules* **2021**, *26*, 6893.
- (23) Bax, A.; Lerner, L. Two-Dimensional Nuclear Magnetic Resonance Spectroscopy. *Science* **1986**, *232*, 960–967.
- (24) Kessler, H.; Gehrke, M.; Griesinger, C. Two-Dimensional NMR Spectroscopy: Background and Overview of the Experiments [New Analytical Methods (36)]. *Angew. Chem. Int. Ed.* **1988**, *27*, 490–536.
- (25) Hamm, P.; Zanni, M. T. *Concepts and Methods of 2D Infrared Spectroscopy*; Cambridge University Press: New York, 2011.
- (26) Hamm, P.; Helbing, J.; Bredenbeck, J. Two-Dimensional Infrared Spectroscopy of Photoswitchable Peptides. *Annu. Rev. Phys. Chem.* **2008**, *59*, 291–317.
- (27) Biswas, S.; Kim, J. W.; Zhang, X. Z.; Scholes, G. D. Coherent Two-Dimensional and Broadband Electronic Spectroscopies. *Chem. Rev.* **2022**, *122*, 4257–4321.

- (28) Fuller, F. D.; Ogilvie, J. P. Experimental Implementations of Two-Dimensional Fourier Transform Electronic Spectroscopy. *Annu. Rev. Phys. Chem.* **2015**, *66*, 667–690.
- (29) Mukamel, S. *Principles of Nonlinear Optical Spectroscopy*; Oxford University Press, New York, 1999.
- (30) Deng, R.-Q.; Liu, C.-G.; Yao, Y.-X.; Jin, J.-Y.-R.; Zhang, H.-Y.; Song, Y.; Ai, Q. Anomalous Reduced Homogeneous Broadening of Two-Dimensional Electronic Spectroscopy at High Temperature by Detailed Balance. *Phys. Rev. A* **2024**, *109*, 052801.
- (31) Cho, M. Nonlinear Response Functions for the Three-Dimensional Spectroscopies. *J. Chem. Phys.* **2001**, *115*, 4424–4437.
- (32) Bender, C. M.; Boettcher, S. Real Spectra in Non-Hermitian Hamiltonians Having \mathcal{PT} Symmetry. *Phys. Rev. Lett.* **1998**, *80*, 5243–5246.
- (33) Ashida, Y.; Furukawa, S.; Ueda, M. Parity-Time-Symmetric Quantum Critical Phenomena. *Nat. Commun.* **2017**, *8*, 15791.
- (34) Feng, L.; El-Ganainy, R.; Ge, L. Non-Hermitian Photonics Based on Parity-Time Symmetry. *Nat. Photonics* **2017**, *11*, 752–762.
- (35) Olaya-Castro, A.; Lee, C. F.; Olsen, F. F.; Johnson, N. F. Efficiency of Energy Transfer in a Light-Harvesting System under Quantum Coherence. *Phys. Rev. B* **2008**, *78*, 085115.
- (36) Celardo, G. L.; Borgonovi, F.; Merkli, M.; Tsifrinovich, V. I.; Berman, G. P. Super-radiance Transition in Photosynthetic Light-Harvesting Complexes. *J. Phys. Chem. C* **2012**, *116*, 22105–22111.
- (37) Nesterov, A. I.; Berman, G. P.; Bishop, A. R. Non-Hermitian Approach for Modeling of Noise-Assisted Quantum Electron Transfer in Photosynthetic Complexes. *Fortschr. Phys.* **2013**, *61*, 95–110.

- (38) Jones, J.; Hore, P. Spin-Selective Reactions of Radical Pairs Act as Quantum Measurements. *Chem. Phys. Lett.* **2010**, *488*, 90–93.
- (39) Haberkorn, R. Density Matrix Description of Spin-Selective Radical Pair Reactions. *Mol. Phys.* **1976**, *32*, 1491–1493.
- (40) Maeda, K.; Henbest, K. B.; Cintolesi, F.; Kuprov, I.; Rodgers, C. T.; Liddell, P. A.; Gust, D.; Timmel, C. R.; Hore, P. J. Chemical Compass Model of Avian Magnetoreception. *Nature* **2008**, *453*, 387–390.
- (41) Fang, Y. N.; Shen, Y.; Ai, Q.; Sun, C. P. Negative Refraction in Möbius Molecules. *Phys. Rev. A* **2016**, *94*, 043805.
- (42) Lemmer, A.; Cormick, C.; Schmiegelow, C. T.; Schmidt-Kaler, F.; Plenio, M. B. Two-Dimensional Spectroscopy for the Study of Ion Coulomb Crystals. *Phys. Rev. Lett.* **2015**, *114*, 073001.
- (43) Fleischhauer, M.; Imamoglu, A.; Marangos, J. P. Electromagnetically Induced Transparency: Optics in Coherent Media. *Rev. Mod. Phys.* **2005**, *77*, 633–673.
- (44) Liu, G.-Y.; Sizhuk, A. S.; Dorfman, K. E. Selective Elimination of Homogeneous Broadening by Multidimensional Spectroscopy in the Electromagnetically Induced Transparency Regime. *J. Phys. Chem. Lett.* **2020**, *11*, 5504–5509.
- (45) Chen, Y.-Y.; Ye, C.; Zhang, Q.; Li, Y. Enantio-Discrimination Via Light Deflection Effect. *J. Chem. Phys.* **2020**, *152*, 204305.
- (46) Arenas, B. E.; Gruet, S.; Steber, A. L.; Schnell, M. A Global Study of the Conformers of 1,2-Propanediol and New Vibrationally Excited States. *J. Mol. Spectrosc.* **2017**, *337*, 9–16.
- (47) Lovas, F.; Plusquellic, D.; Pate, B. H.; Neill, J. L.; Muckle, M. T.; Remijan, A. J. Microwave Spectrum of 1,2-Propanediol. *J. Mol. Spectrosc.* **2009**, *257*, 82–93.

- (48) Cai, M.-R.; Ye, C.; Dong, H.; Li, Y. Enantiodetection of Chiral Molecules via Two-Dimensional Spectroscopy. *Phys. Rev. Lett.* **2022**, *129*, 103201.
- (49) Patterson, D.; Doyle, J. M. Cooling Molecules in a Cell for FTMW Spectroscopy. *Mol. Phys.* **2012**, *110*, 1757–1766.
- (50) Eibenberger, S.; Doyle, J.; Patterson, D. Enantiomer-Specific State Transfer of Chiral Molecules. *Phys. Rev. Lett.* **2017**, *118*, 123002.
- (51) Gelin, M. F.; Chen, L.; Domcke, W. Equation-of-Motion Methods for the Calculation of Femtosecond Time-Resolved 4-Wave-Mixing and N-Wave-Mixing Signals. *Chem. Rev.* **2022**, *122*, 17339–17396.